# Electroluminescence from Single-Walled Carbon Nanotubes with Quantum Defects

Min-Ken Li, Adnan Riaz, Martina Wederhake, Karin Fink, Avishek Saha, Simone Dehm, Xiaowei He, Friedrich Schöppler, Manfred M. Kappes, Han Htoon, Valentin N. Popov, Stephen K. Doorn, Tobias Hertel, Frank Hennrich, and Ralph Krupke*

ABSTRACT: Individual single-walled carbon nanotubes with covalent sidewall defects have emerged as a class of photon sources whose photoluminescence spectra can be tailored by the carbon nanotube chirality and the attached functional group/molecule. Here we present electroluminescence spectroscopy data from single-tube devices based on (7, 5) carbon nanotubes, functionalized with dichlorobenzene molecules, and wired to graphene electrodes. We observe electrically generated, defect-induced emissions that are controllable by electrostatic gating and strongly red-shifted compared to emissions from pristine nanotubes. The defect-induced emissions are assigned to excitonic and trionic recombination processes by correlating electroluminescence excitation maps with electrical transport and photoluminescence data. At cryogenic conditions, additional gate-dependent emission lines appear, which are assigned to phonon-assisted hot-exciton electroluminescence from quasi-levels. Similar results were obtained with functionalized (6, 5) nanotubes. We also compare functionalized (7, 5) electroluminescence data with photoluminescence of pristine and functionalized (7, 5) nanotubes redox-doped using gold(III) chloride solution. This work shows that electroluminescence excitation is selective toward neutral defect-state configurations with the lowest transition energy, which in combination with gate-control over neutral versus charged defect-state emission leads to high spectral purity.

KEYWORDS: carbon nanotubes, defects, graphene, electroluminescence, photoluminescence, excitons, doping
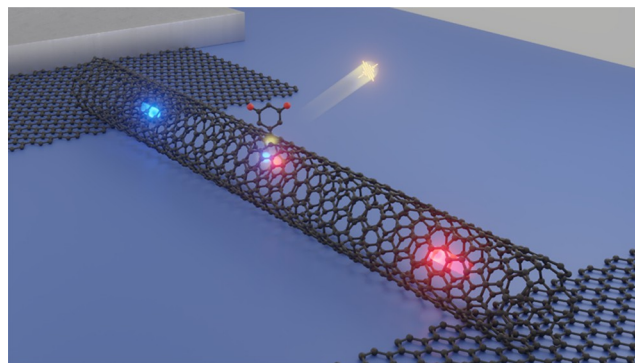
INTRODUCTION

Photonic quantum technology has been widely explored in recent years with the aim to improve the current limitation in quantum information processing, such as quantum computing[1] and quantum cryptography.[2] Single-photon sources are indispensable components of these technologies, and tremendous effort has been devoted to the integration of low-dimensional nanoscale solid-state sources[3,4] such as color centers in diamond,[5] quantum dots,[6] and single molecules.[7] However, realizing electrical excitation, room temperature operation, and stable emission in technologically relevant telecom bands (1.3−1.6 μm) of optical fiber-based quantum communications remains a formidable challenge for these emitters. Semiconducting single-walled carbon nanotubes (SWCNTs), on the other hand, possess many desirable properties for photonic applications,[8] especially structure-dependent, excitonic emission wavelengths, that can be tuned from 850 nm to 2 μm, and which can be triggered optically and electrically. Photon antibunching in photoluminescence,[9] as

well as electroluminescence,[10] have been demonstrated. However, small luminescence quantum yields, mainly owing to the low-lying optically forbidden "dark" exciton states[11] and undesired quenching sites,[12] as well as the cryogenic temperatures required to achieve single-photon emission behavior still frustrate the development of carbon nanotubes as quantum-light sources.

Recent progress has shown how the introduction of quantum dot-like (0D) defects to the sidewalls of carbon nanotubes through low-level oxygen,[13] alkyl,[14,15] or covalent aryl sp³ functionalization[16,17] not only significantly enhance the photoluminescence emission efficiency (from <1% up to
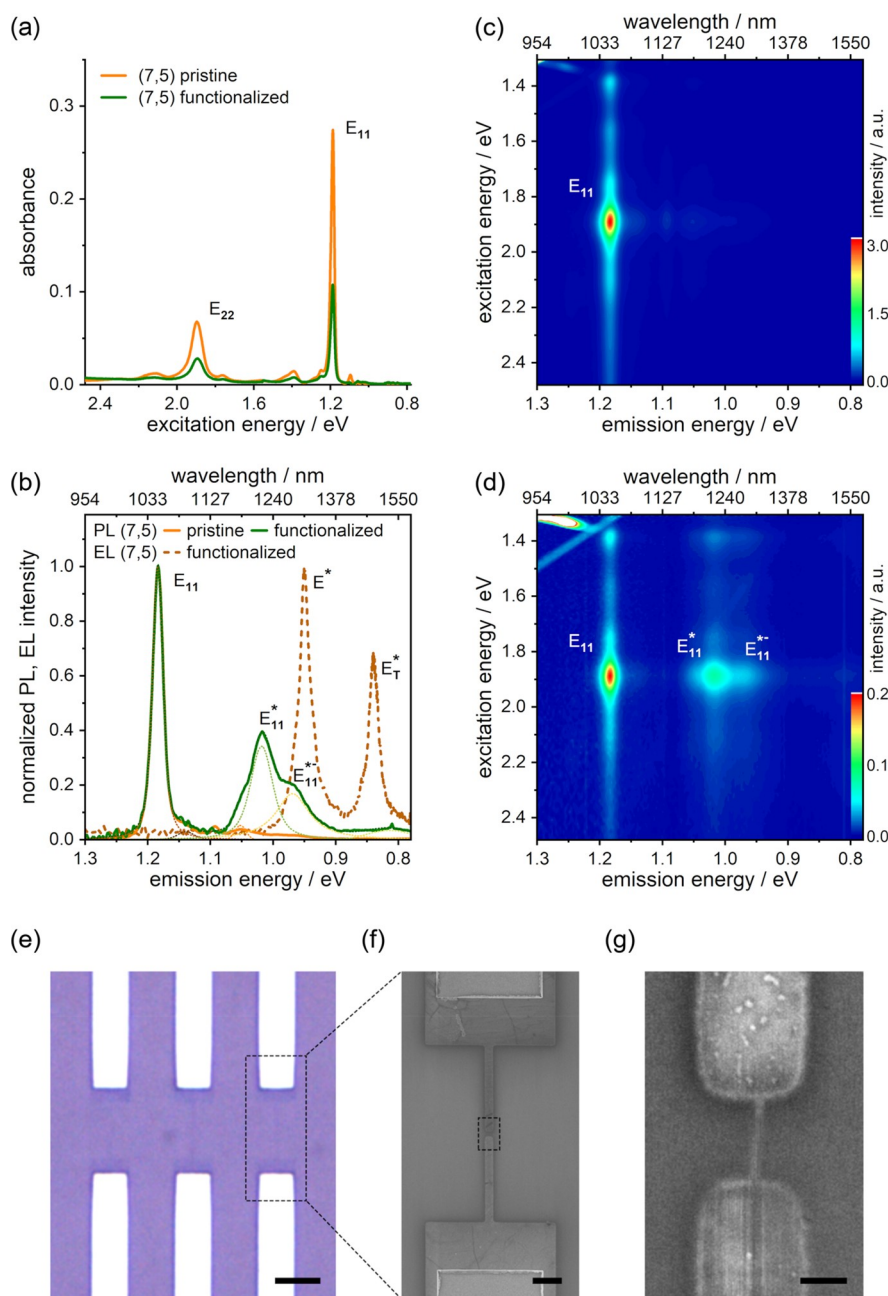
Figure 1. (a) Absorption spectra of pristine and 3,5-dichlorobenzene-functionalized polymer-wrapped (7, 5) carbon nanotubes dispersed in toluene. The corresponding photoluminescence spectra excited at E_{22} (1.89 eV) are shown in (b). Photoluminescence excitation map of the suspension with pristine and functionalized (7, 5) are shown in (c) and (d), respectively. E_{11} emission and the red-shifted defect-state emission ($E_{11}*$ and $E_{11}*^{-}$) are labeled. The electroluminescence (EL) spectrum of a single-tube device, measured at 40 nA source-drain current and 4 V gate-voltage at 77 K, is overlaid in (b). The defect-state EL emission ($E*$) is at the similar emission energy as $E_{11}*^{-}$ emission in the PL measurement. $E*_{T}$ is the trionic defect-state EL emission, as discussed in the text. The PL spectra were fitted with Voigt function. All data except electroluminescence spectrum recorded at RT. (e−g) Optical and scanning electron microscopy images of a single-tube device with graphene electrodes, taken after electroluminescence characterization. Scalebar equals (e) 5 μm, (f) 1 μm, and (g) 100 nm.

28%)[16,18] but also redshift the photoluminescence emission wavelength deeper into the near-infrared regime. The sp^3 defects, which trap mobile excitons in potentials of 100−300 meV depth, extend the single-photon emission characteristics of carbon nanotube to room temperature[19,20] and may thereby facilitate their use in sensing and imaging applications. From an applied research perspective, an on-chip source with electrical controllability is an important component of applications. Although extensive studies have focused on understanding the emission characteristics of functionalized

SWCNTs, mostly through optical means, only a little has been reported regarding electrically driven luminescence. Xu et al. showed electroluminescence from a functionalized SWCNT film network via an impact excitation mechanism.[21] Zorn et al. demonstrated the interplay between charge transport and electroluminescence from functionalized SWCNT networks.[22] However, an electroluminescence study of functionalized SWCNT at the single tube level, which is crucial for quantum photonics, has so far not been reported. Also, despite the observation of electroluminescence from localized trions in
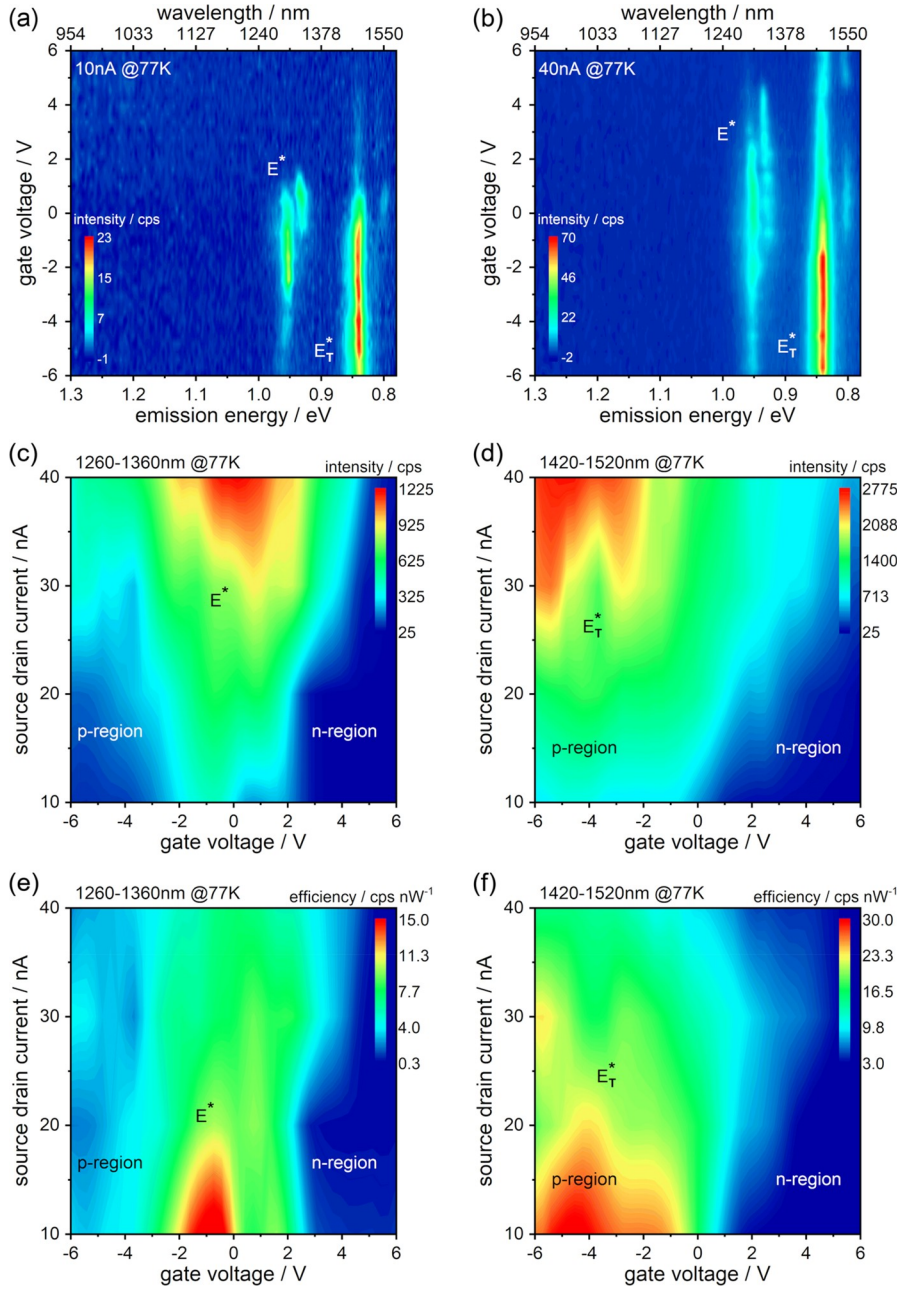
Figure 2. Electroluminescence (EL) spectral intensity versus gate voltage of a functionalized (7, 5) device measured at (a) 10 nA and (b) 40 nA source-drain current. Excitonic and trionic defect-state emissions are indicated as E^* and E^*_T, respectively. (c) Integrated excitonic and (d) trionic defect-state emission intensity versus source-drain current and gate-voltage (excitonic range: 1260−1360 nm; trionic range: 1420−1520 nm). The efficiency of (e) excitonic defect-state emission and (f) trionic defect-state emission is given in count rate/electrical power. Regions of electron (n) and hole (p) conduction are labeled. The excitonic defect-state emission appears near the charge neutrality region, whereas the trionic defect-state emission is dominant in the p-region. Data recorded at 77 K.

previous works,[21] a comprehensive understanding of the formation condition of trions and interrelation between electrical transport and emission behavior is still missing.

In this work, we fabricated dichlorobenzene-functionalized (7, 5) SWCNT field-effect transistors with graphene electrodes and demonstrated defect-induced excitonic and trionic electroluminescence through carrier recombination at the single tube level. The spectral weight of defect-induced emission was tuned by electrostatic gating and further correlated with electrical transport measurements. At cryogenic temperature and under certain gating conditions, unexpected emission lines were observed which we could attribute to phonon-mediated

hot-exciton electroluminescence. Finally, electroluminescence and photoluminescence from SWCNTs with and without functionalization were compared to help better understand the intrinsic and defect-related emission behavior.

RESULTS AND DISCUSSION

Carbon nanotube suspensions were prepared from CoMoCAT single-walled carbon nanotubes by polyfluorene (PFO) polymer-wrapping in toluene, and length sorted and purified by gel filtration chromatography.[23] The functionalization reaction was carried out by adding 3,5-dichlorophenyldiazonium tetrafluoroborate to the suspension and heating close to
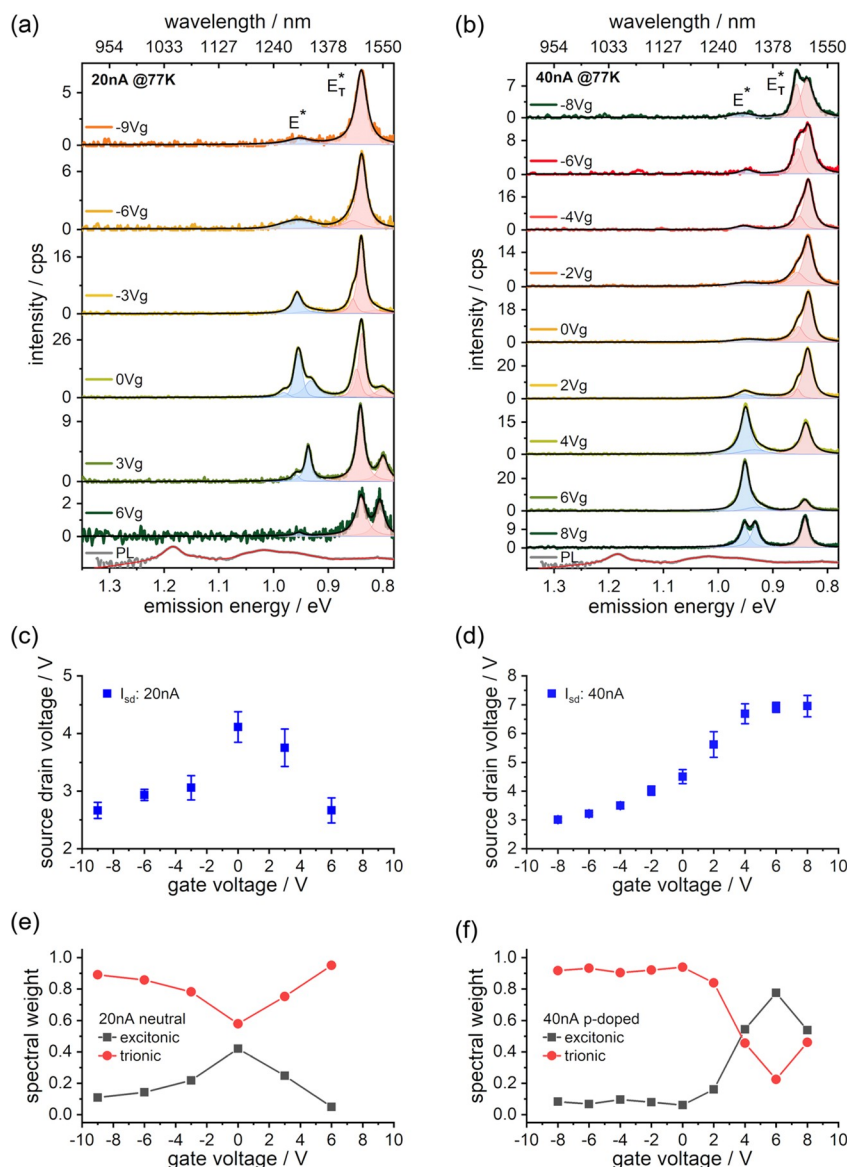
Figure 3. Gate-voltage dependence of EL spectra of functionalized (7, 5) devices with different unintentional doping: in (a,c,e) channel is undoped at zero gate voltage, in (b,d,f) channel is hole-doped. Excitonic and trionic defect-state peaks are labeled as E* and E*$_T$. The spectra were fitted with Voigt functions. The PL spectrum of the suspension is shown for comparison and plotted on logscale. (c,d) Transport data. Maximum source-drain voltage corresponds to charge-neutrality/off-state and is reached in (c) at zero gate voltage and in (d) at 6 V gate voltage. (e,f) Relative spectral weight of excitonic and trionic defect-state emission from integrated E* and E*$_T$ lines. Data recorded at 77 K.

the boiling point of toluene for an hour in a dark environment. Photoluminescence measurements were performed directly following the functionalization process to confirm the successful formation of sp^3 defects. For details, we refer to the Methods section. Absorption spectra of the polymer-wrapped pristine and functionalized (7, 5) carbon nanotube suspensions with the prominent E_{11} and E_{22} excitonic transitions are shown in Figure 1a. From the integrated intensities we have determined a > 99% chiral purity with minor (6, 5) and (7, 6) impurities.

After functionalization, the E_{11} and E_{22} peak absorbance has dropped to ≈60% partially due to dilution. Figure 1c,d shows the corresponding photoluminescence excitation maps of the pristine and functionalized (7, 5) nanotube suspensions. The E_{11} excitonic emission of the (7, 5) tubes occurs at 1.18 eV (1050 nm) under E_{22} excitation at 1.89 eV (657 nm). Impurity species become visible only for logarithmic intensity scaling

(Supporting Information (SI) Figure S1). The additional functionalization-induced emission bands (denoted here as $E_{11}*$ and $E_{11}*^-$) are visible in Figure 1b,d, similar to previous reports on aryl sp^3-functionalized nanotubes, where $E_{11}*$ and $E_{11}*^-$ are associated with the formation of sp^3 defects and exciton localization at deep traps.[20] Compared to the intrinsic E_{11} emission from mobile excitons, the functionalization-induced emission emerges over a rather broad energy range, which has been attributed to spectral diversity in chiral nanotubes caused by multiple covalent binding configurations for an aryl group to the nanotube lattice.[24,25]

From a diluted suspension, individual functionalized (7, 5) nanotubes—on average 500 nm long (SI Figure S2)—were deposited onto source-drain graphene electrode with 100 nm gap via DC-dielectrophoresis[26] (see Methods section). The deposition conditions were adjusted to obtain single-tube devices (see Figure 1e−g). The devices were electrically wire

bonded, in a field-effect transistor configuration using the p-Si as back-gate, and mounted into the optical cryostat of our near-infrared optical microscopy and spectroscopy setup.[27] The cryostat was evacuated to 10^{-7} mbar and the samples were vacuum annealed and subsequently cooled down to 77 or 4 K to suppress gate-voltage hysteresis.[27] The devices were biased in constant-current mode to obtain stable light emission and bias-independent electrostatic doping of the nanotube channel via the gate voltage.[27] The light emitted from the SWCNT devices was dispersed via an imaging spectrograph grating onto a linear InGaAs photodiode array with a wavelength range from 950 to 1610 nm. All spectra were calibrated by the relative spectral sensitivity of the setup.[27]

Electroluminescence from Functionalized (7, 5). Figure 2a,b shows maps of electroluminescence (EL) spectral intensity versus gate-voltage from a representative functionalized (7, 5) device, measured at 10 and 40 nA source-drain current and 77 K. Spectra were recorded in 42 subsequent steps of gate-voltage sweeping with an integration time of 10 s for each spectrum at a given constant-current bias. The corresponding source-drain voltage was continuously recorded to monitor the doping level of the nanotube channel. The EL maps show that the electroluminescence spectral weight is entirely red-shifted from the intrinsic E_{11} emission at ~1.18 eV (1050 nm) to new emission lines at ~0.95 eV (1305 nm) and ~0.84 eV (1476 nm) marked as E* and E*$_T$, and that these lines can be switched ON and OFF with the back-gate voltage. We emphasize that the red-shifts of 230 and 340 meV are so large that we can rule out a contribution of the (7, 5) intrinsic trionic emission, which we have measured previously with pristine (7, 5) and which appears red-shifted by 160 meV at ~1.02 eV (1215 nm).[27] An example spectrum with the trionic emission of a pristine (7, 5) is also presented in Figure 6c.

When comparing the positions of the E* and E*$_T$ with the photoluminescence spectrum of functionalized (7, 5) nanotubes (Figure 1b), we find that the electroluminescent emission occurs in the broad region of functionalization-induced photoluminescent emissions that have been assigned previously to the E_{11}*$^-$ or E_{11}** defect-state emissions of aryl-functionalized nanotubes,[24,25,28,29] and to the corresponding trion.[30] Therefore, the two new emission lines must be defect-induced. To understand the nature of the two distinctive defect lines it is instructive to realize that the emission at ~0.95 eV (E*) is predominant in the gate-voltage range of 2 to −3 V, whereas the emission at ~0.84 eV (E*$_T$) is predominant from 0 to −6 V, for all current biasing conditions. This gate-induced switching of emission lines is similar to the previously studied gate-induced switching between excitonic and trionic emission from pristine carbon nanotubes.[27] In analogy, we assign the two defect-induced lines to an excitonic defect-state emission (E*) and the corresponding trionic defect-state emission (E*$_T$). This assignment will become further substantiated when correlating the electroluminescence spectra with transport data.

To determine under which biasing and gating conditions defect-mediated excitons and trions would form and radiatively recombine, we have integrated the intensities associated with the excitonic defect-state emission (1260−1360 nm) and the trionic defect-state emission (1420−1520 nm) over the wavelength and plotted against source-drain current and gate-voltage in Figure 2c,d. The electroluminescence excitation maps reveal distinctive regions in which trapped excitons and trions are formed and emit light. From the corresponding source-drain voltage map (SI Figure S3a), we identify the gate-voltage regions where the nanotube channel is p-doped, n-doped, and charge neutral.[27] These regions are indicated in Figure 2c−f and are used to correlate light emission with charge transport. Figure 2c shows that the excitonic defect-state emission is dominant in the gate-voltage range of ±2 V, where charge neutrality is met (between p-region and n-region). Such an intensity maximum at charge neutrality is a unique signature of exciton formation via carrier recombination and excludes unipolar impact excitation.[31−33,27]

Likewise, trionic emission occurs in a limited gate-voltage range, where electrons and holes are injected but the channel is significantly doped.[27] In Figure 2d the positive trion appears in the p-region at gate voltages below −2 V. The appearance of the negative trion is shown later. To identify conditions with enhanced efficiency of defect-state emission we have normalized the electroluminescence excitation maps with the corresponding electrical power dissipation map (SI Figure S3b) and created in Figure 2e,f maps of emission efficiency for the defect-state emissions. The excitonic and trionic emission efficiencies are maximized at low current bias, where the gate-voltage range for the formation of excitons and trions is narrow.

Influence of Gating and Doping. So far we have described the general behavior of defect-induced emission on the biasing conditions. Upon closer inspection, one finds that the spectral evolution as a function of gate voltage is more complex, as is shown for two sets of data in Figure 3a,b. We observe that the E* and E*$_T$ emission lines consist of more than one peak and are often split into pairs of peaks that could be fitted with Voigt profiles (details in SI Figure S4). In addition to the overall gate dependence discussed above, we observe that the relative intensity of the components varies with the gate voltage, whereas the peak positions within one set of data remain constant. The energy scale of the peak splitting is about 18 meV and much smaller than the ~110 meV energy difference between E* and E*$_T$. The nature of the peak splitting could be caused by two different defect sites on the same tube with the same binding configuration but existing in different local chemical/dielectric environments.[24] The energy difference between the defect-exciton E* and the defect-trion E*$_T$ is similar to recent chemical doping studies with defective nanotubes.[30] Apart from general reproducibility, the data in Figure 3a,b are not identical. For example, an additional peak appears below the energy of the E*$_T$ for positive gate voltages, and an additional set of data (SI Figure S5) shows E*$_T$ absent while the splitting of E* is observed. Some of the differences are due to unintentional doping of the nanotube channel, for instance by charge trapping in the substrate.

Doping can be detected from the transport data in Figure 3c,d, where the source-drain voltage is plotted versus the gate voltage at constant current. The nanotube channel is charge-neutral when the source-drain voltage is at maximum, which is reached in Figure 3a,c at zero gate voltage. In contrast, in Figure 3b,d the maximum source-drain voltage and charge-neutrality are reached at +6 V. At zero gate voltage the nanotube channel is p-doped. The excitonic defect-state emission reflects this difference in residual doping since E* becomes predominant at the respective gate voltages where the nanotube channel is charge neutral. The trionic defect-state emission is sensitive to doping in the same manner. E*$_T$ intensifies when the channel hosts excess charges that are
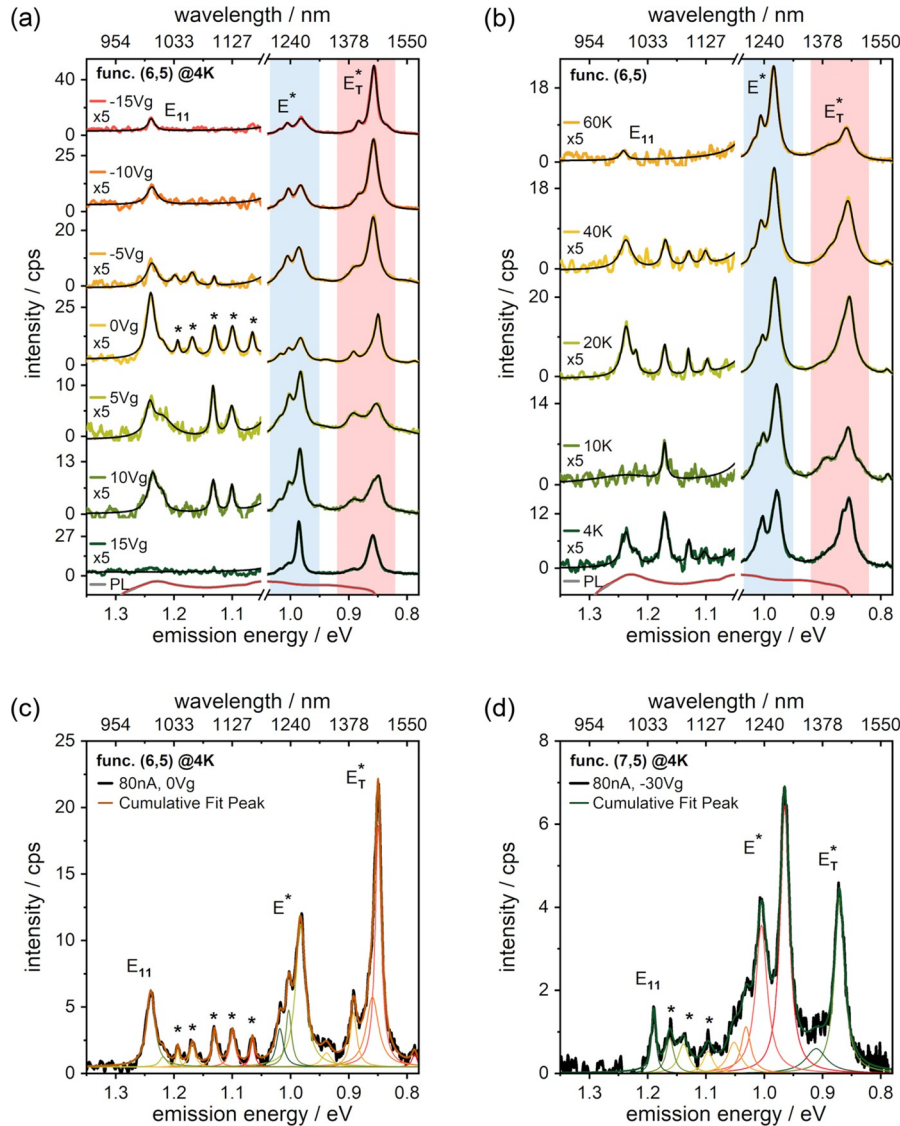
Figure 4. EL spectra of functionalized (6, 5) and (7, 5) devices at very low temperatures. (a) Spectra of functionalized (6, 5) measured at 4 K over a wide gate-voltage range. Intrinsic E_{11} emission and additional starred peaks become visible at charge neutrality. Intensity scaled by factor 5 above 1.05 eV for clarity and PL spectrum of suspension added in logscale. (b) Temperature dependence of EL spectra from functionalized (6, 5). (c) Enlarged view on functionalized (6, 5) spectrum at zero gate-voltage. Multipeak fitting with Lorentzian. (d) EL spectrum of functionalized (7, 5) device recorded at 4 K. Excitonic and trionic defect-state peaks are labeled as E^* and E^*_T.

required for the trion formation. This mutual dependence between E^* and E^*_T and the gate-voltage at charge-neutrality is better captured in Figure 3e,f, where the relative spectral weight of the integrated excitonic and trionic defect-state emission intensity is plotted versus the gate voltage. The same behavior is observed in more sets of data (SI Figure S5).

Comparative EL Data from Functionalized (6, 5). The observations that we made are not unique to the (7, 5) nanotube chirality, the type of polymer, or electrode material. Similar measurements were performed on 3,5-dichlorobenzene-functionalized, PFO-BPy wrapped (6, 5) nanotubes wired to Pd source-drain electrodes (details in Methods section). We observe excitonic and trionic defect-state emissions from functionalized (6, 5) that are similar to the functionalized (7, 5) SWCNTs, with chirality-related shifts of peak positions. In Figure 4a we see that the E^* and E^*_T peaks, highlighted in blue and red, respectively, respond to the gate-voltage in the same way. Also, a splitting of the E^* and E^*_T lines is visible. As

before, we added the photoluminescence data from the corresponding dispersion in logarithmic scaling. For the functionalized (6, 5) SWCNTs we also see that the electroluminescent excitonic defect-emission lines fall into the broad region of functionalization-induced photoluminescence (more data in SI Figure S6). The data shown in Figure 4a was recorded at 4 K and interestingly, the intrinsic E_{11} emission is visible in addition to the defect-state emission. The E_{11} emission becomes weaker with increasing temperature (Figure 4b) and disappears above 60 K (SI Figure S7). We believe that the localization of excitons at very low temperatures by shallow traps plays a role.[9,34] Shallow traps, for example, induced by interaction with the polymer or substrate surface, do not lead to a significant change of the emission wavelength but can give rise to single-photon emission.[9,27] Such a trapping of mobile E_{11} excitons by shallow traps makes the probability of reaching a deep defect-induced trap less likely and the shift of spectral weight from E_{11} to the defect-
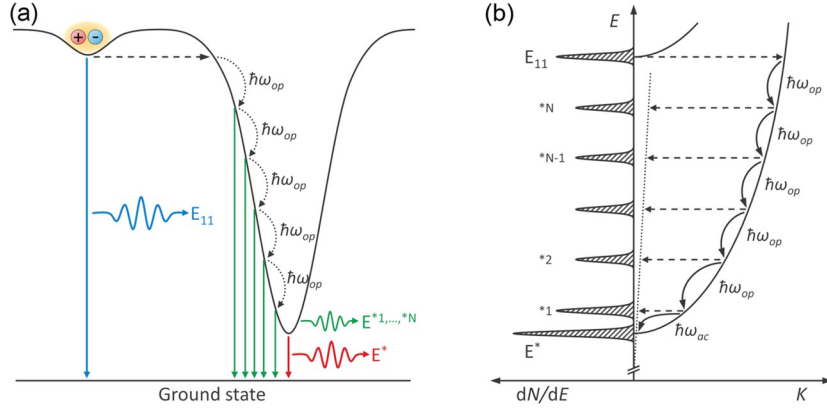
Figure 5. (a) Schematic depiction of hot-exciton injection from a shallow trap into a deep trap and the subsequent energy relaxation by optical phonon emission. The transition energies for the shallow trap (E_{11}), the deep trap (E^*), and from the hot-exciton quasi-levels ($E^{*1,\cdots,*N}$) are indicated. (b) Simplified model of exciton kinetic energy relaxation. The parabolic curves describe the energy E versus momentum K dispersions of the E^* defect exciton and of the E_{11} exciton, which is converted into a hot exciton at the defect (right-headed dashed arrow). The full arrows show the optical ($\hbar\omega_{op}$) and acoustic ($\hbar\omega_{ac}$) phonon relaxation processes. The left-headed dashed arrows indicate the momentum scattering that is required for radiative recombination via the photon dispersion (dotted line). The left part in (b) shows the exciton distribution on energy with the hot-exciton quasi-levels *1,*2,..,*N.

state emission is reduced. Vice versa, with rising temperature the detrapping from shallow traps increases,[9] and the probability for mobile excitons to get trapped by the defect deep trap becomes large, provided the nanotube length is comparable or shorter than the exciton diffusion length,[35] as is the case in this work. We observe the localization of E_{11} excitons also with functionalized (7, 5) nanotubes and show in Figure 4d a measurement at 4 K, where the intrinsic E_{11} emission is visible together with the defect-state emissions. We have one set of functionalized (7, 5) data where we observe the E_{11} emission also at 77 K (SI Figure S5), which we attribute either to the presence of a deeper shallow trap or to a second tube without a defect.

Low-Temperature Emission Lines. We now discuss the appearance of a series of new peaks between the E_{11} and the defect emission lines, seen in Figure 4a−d. The peaks (marked with stars) become only visible at very low temperatures when the intensity of the E_{11} emission is comparable to the defect emission. This is shown in Figure 4a,c for functionalized (6, 5) SWCNTs, and a similar case is presented in Figure 4d for functionalized (7, 5) SWCNTs. We have introduced in Figure 4a,b an x-axis break (0.01 eV), and rescaled the y-axis in the energy range >1.05 eV to allow a clearer distinction of different peaks. Figure 4b shows that the starred peaks are temperature-dependent, and disappear simultaneously with the E_{11} emission between 40 and 60 K. In addition, we see in Figure 4a that complete suppression of the starred peaks can be induced by applying large gate voltages. Also, in this case, the correlation with the E_{11} intensity is visible and we conclude that the starred peaks are associated with the formation of weakly localized E_{11} excitons in proximity to a defect. We note that functionalization is essential since we do not observe the starred peaks on pristine nanotubes.[27] Of the 15 devices that we examined, all devices showed defect-state emission, and for five devices we were able to find a gate voltage range at 4 K where the additional peaks appear. For the data in Figure 4c,d we have fitted the new peaks to Lorentzian functions and analyzed the spacing in energy between neighboring peaks (see SI Figure S8). We find that the energy spacing is approximately equidistant and the average spacing in energy is 34.9 ± 8.0 meV and 31.2 ± 9.9 meV for functionalized (6, 5) and (7, 5)

nanotubes, respectively, which is close to the radial breathing mode (RBM) energies of the (6, 5) and (7, 5) nanotubes, 38 and 35 meV, respectively.[22,36−40] Therefore, and because of the correlation of the peaks with the E_{11} intensity, we assume that the series of peaks is related to a coupling between the E_{11} exciton and RBM phonons.

In carbon nanotubes, distinct phonon sidebands have been described by Lefebvre et al.,[41] who assigned peaks appearing below 20 K to replicas of low-energy squashing modes of the nanotube. The energy spacing was 2−3 meV. Low-energy wings, often observed in carbon nanotube photoluminescence are typically several meV wide and have been assigned to coupling to low-energy phonons of nanotubes,[42] while spectral gaps in the low-energy wing were attributed to phonon confinement.[43] Recently, Nutz et al. assigned multiple peaks in the low-energy photoluminescence wing of PFO decorated nanotubes to phonon replicas of the vibrational modes of the PFO monomer.[44] These modes have a characteristic energy scale of ∼2 meV. In our experiment, the energy spacing is much larger. We have performed density functional theory (DFT) calculations of the 3,5-dichlorobenzene molecule covalently bound to a graphene flake and performed a normal-mode frequency analysis.[45] In the relevant energy range we found normal-mode frequencies around 48 meV, which lead to a deformation of the local graphene lattice that is absent in simulations without the molecule (SI Figure S9). Given that our DFT calculations are only an approximation to the problem we cannot rule out that vibrational modes of the functional group might also play a role, but the energy spacing of the peaks fits much better to the RBM energies.

The question arises why the starred peaks only appear when the E_{11} exciton becomes weakly localized by a shallow trap in the vicinity of a defect-induced deep trap. The explanation that we consider is presented in Figure 5a. It depicts the conversion of a weakly trapped E_{11} exciton into a deeply trapped E^* exciton via the emission of multiple optical phonons. This process can be seen in analogy to the phonon-mediated relaxation of hot excitons in optically excited II−VI semi-conductors.[46−49] The mechanism that leads to multiple emission lines, located energetically below the hot-exciton quasi-level, has been described in great detail by Permogor-
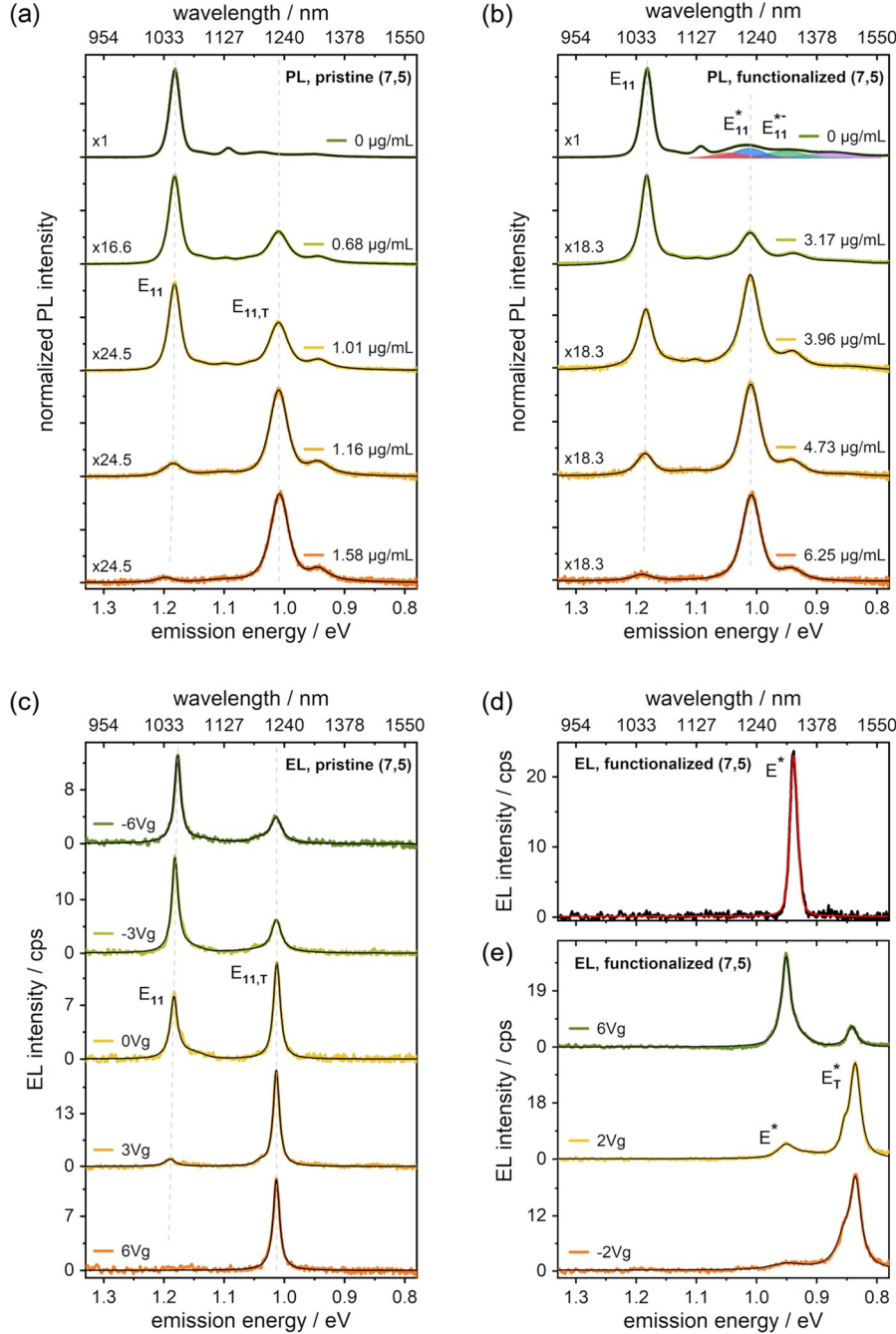
Figure 6. Comparison of photoluminescence (PL) spectra of redox-doped (a) pristine (7, 5) and (b) functionalized (7, 5) suspensions with electroluminescence (EL) spectra of gate-voltage controlled (c) pristine (7, 5) and (e) functionalized (7, 5) single-tube devices. The AuCl$_3$ concentration in (a) and (b) increases from top to bottom. Intensity scaling factors are given. Excitonic E$_{11}$ and trionic E$_{11,T}$ emissions are labeled. (b) The defect-state emissions E$_{11}$* and E$_{11}$*$^-$ are observed for the functionalized (7, 5) at zero doping. Data recorded at RT and under excitation at 1.91 eV/650 nm. (c) EL spectra of pristine (7, 5) single-tube devices measured at 77 K. The peak positions of the gate-voltage controlled excitonic E$_{11}$ and trionic E$_{11,T}$ emissions are marked by dashed lines in the PL spectra. (d) EL defect-state emission E* with high spectral purity under optimum source-drain current (3 nA) and gate-voltage (6 Vg) conditions at 77 K. (e) EL spectra of functionalized (7, 5) single-tube device recorded at 40 nA source-drain current and 77 K. All spectra were fitted with Voigt functions.

ov.[50] It requires that the exciton lifetime is short compared to the thermalization processes and that the optical-phonon relaxation rate is larger than the rates of acoustic-phonon relaxation, nonradiative decay, and radiative decay. The generation of hot excitons by excitation with monochromatic light of energy $h\nu$ can then lead to the formation of exciton quasi-levels of energy $E_n = h\nu - n\hbar\omega_{op}$ (n is an integer). In our case, shown in Figure 5b, hot excitons are formed from the

electrically generated E$_{11}$ excitons in the vicinity of the defect by phonon/defect scattering. In this picture, hot-exciton quasi-levels will then form at energies $E_n = E_{11} - n\hbar\omega_{op}$, and $\hbar\omega_{op}$ would correspond to the RBM energy. The population of these levels can be calculated with balance equations. Under stationary conditions, the populations P_N and P_{N-1}, of the levels N and $N-1$, can be derived from[50]

$$dP_N/dt = A - P_N \cdot (W_{nrad} + W_{op}) = 0,$$

$$dP_{N-1}/dt = P_N \cdot W_{op} - P_{N-1} \cdot (W_{nrad} + W_{op}) = 0,$$

with A, the hot-exciton generation rate, W_{nrad}, the nonradiative decay rate, and W_{op}, the rate for relaxation with optical phonon emission. The populations of P_N and P_{N-1} are then given by

$$P_N = A/(W_{nrad} + W_{op}),$$

$$P_{N-1} = P_N \cdot W_{op}/(W_{nrad} + W_{op}).$$

With the assumption that $W_{op} \gg W_{nrad}$ it follows that $P_N \approx P_{N-1}$. Similar results can be obtained for the other hot exciton quasi-levels and the population of these levels would approximately be the same. For the radiative recombination from the quasi-levels, a scattering process is required that accounts also for the momentum mismatch (as indicated in Figure 5b). This could be satisfied by the optical phonon scattering itself, provided the phonon dispersion bandwidth is small. We note that the RBM bandwidth is found to scale inversely with the unit cell size,[51] and for the chiral (6, 5) and (7, 5) nanotubes with large unit cells, the RBM bandwidth is expected to be small. In the case of the (6, 5) nanotube, the RBM frequency, calculated within a tight-binding model, shows only a slight variation of about 1% throughout the Brillouin zone of the nanotube,[52] and therefore the RBM bandwidth is small enough to consider the RBM frequency as a constant. To identify the piece of the RBM branch, relevant to the relaxation processes, we use the E_{11} exciton mass, derived within a tight-binding model, and find that the exciton states in the energy range from E* to E_{11} (Figure 5b) have wavevectors in the first Brillouin zone. The selection rules for exciton–phonon scattering then limit the wavevectors of the scattering phonons of the RBM branch to the latter zone too, where the RBM frequency is approximately constant. This result is in excellent agreement with the measured almost equidistant starred peaks for this nanotube. Similar arguments can be provided for the (7, 5) nanotube as well.

The above scenario nicely explains our observation that the starred peaks are approximately equidistant, have similar intensities, and are seen only for nanotubes with defects. The quenching of the emission intensity with increasing temperature is expected for the hot-exciton luminescence model because of the decreasing hot exciton lifetime due to an increasing nonradiative decay probability at elevated temperatures. We exclude that the starred peaks are due to electron–phonon-coupling induced sideband phonon-replicas because even a very large Huang–Rhys parameter could not explain the intensity distribution.[53] We, therefore, conclude, that the new peaks can be assigned to hot-exciton quasi-levels and can be considered as a signature of hot-exciton (electro)luminescence. We note that multiphonon Raman scattering, which can be triggered by optical excitation,[50,54] can be excluded in our experiment due to the electrical excitation. Besides, the approximately equal population of the quasi-levels and the temperature dependence would not fit a Raman process.[50]

Photoluminescence from Chemically Doped Nanotubes. In this last section, we discuss the assignment of the electroluminescence (EL) defect peaks E* to the photoluminescence (PL) defect peak (E_{11}* and) E_{11}*⁻. Since we observe in the EL experiment a massive influence of the electrostatic gating on the appearance and intensity of the defect peaks, we performed redox doping of pristine and

functionalized (7, 5) dispersions with $AuCl_3$. Figure 6a shows the PL result for the pristine (7, 5) nanotube dispersion. As expected, the E_{11} exciton becomes weaker with hole-doping, and the corresponding trion $E_{11,T}$ increases in intensity and eventually becomes dominant. The doping dependence agrees very well with the EL data from pristine (7, 5) devices (individual nanotubes@77 K), shown in Figure 6c. The E_{11} and $E_{11,T}$ transitions are sharper for the low-temperature EL data, but the peak positions are identical and the evolution of the peak intensities with doping shows the equivalence of electrostatic gating and chemical doping. Also, a blue-shift of E_{11} due to exciton confinement at large doping levels is observed in PL and EL and reproduces previous PL data of redox-doped (6, 5).[55,56] No blue-shift is observed for the $E_{11,T}$ trion.

Figure 6b shows the analogous PL doping study for the functionalized (7, 5) nanotube dispersion. The difference to Figure 1b is due to reabsorption effects in optically dense dispersions, as discussed in SI Figure S10. Overall, the spectra are very similar to the pristine nanotube data, in particular regarding the doping dependence of E_{11} and $E_{11,T}$. The major difference to Figure 6a is visible at zero doping, where additional defect-state PL peaks E_{11}* (blue curve) and E_{11}*⁻ (green curve) appear. Interestingly, the position of E_{11}* matches well to $E_{11,T}$ at a higher doping level, which makes it difficult to determine whether E_{11}* in this data is a signature of a deep exciton trap, or due to trion formation because of functionalization with a charged species. The literature often discusses neutral aryl defects;[24,25] however, evidence for the existence of radical aryl defects giving rise to E_{11}* has also been given.[57,58] It has also been shown that the defect formation is influenced by the condition under which functionalization takes place.[29] A further discussion about the binding configuration and charging state would go beyond the scope of this paper.

If we compare the PL doping study of functionalized (7, 5) with the corresponding EL data in Figure 6e and previous figures we notice that the electroluminescent defect-exciton emission E* occurs in nearly all of our EL data at a wavelength that is close to the E_{11}*⁻ PL emission, which is distinctively of the PL emissions E_{11}* and $E_{11,T}$ (see also Figure 1b). It seems that by electrical excitation the lowest energy state is populated although it is known from PL that defects of different binding configurations can exist on the same tube. This is an important observation in view of chemical attempts to yield tubes in which defect-state emission originates from only a single type of binding configuration.[25,29,59] Beyond such efforts at chemical control, EL may give additional control as it not only seems to naturally access the lowest energy defect configuration but also provides gate control over accessing emission from neutral versus charged defect states. As a result, defect-state electroluminescence spectra with high spectral purity can be obtained under optimized operating conditions (see Figure 6d).

CONCLUSION

We have shown that electroluminescence excitation of single-tube devices with covalent defects triggers emission from neutral defect-state configurations with the lowest transition energy. The intrinsic excitonic and trionic emissions are thereby completely suppressed. With gate-voltage, the emission can be switched from neutral to charged defect-state-emission (defect trion). As a result, a high spectral purity

was reached, which is important for the development of on-chip quantum sources based on functionalized carbon nanotubes. At cryogenic temperatures and under specific bias conditions, the intrinsic excitonic emission becomes visible, and new, nearly equidistant, emission lines appear between the intrinsic and defect emissions. Based on the energetic spacing of the lines, simulations of vibrational modes of the functional group, and correlation with transport measurements, we have assigned these new lines to RBM-phonon mediated hot-exciton electroluminescence. We provide a model for the electrical hot-exciton generation and emission from quasi-levels, analogous to hot-exciton generation in II−VI semi-conductors. Finally, we have compared the electrolumines-cence data with photoluminescence spectra from chemically doped pristine and functionalized nanotubes. For the pristine nanotubes, we find an excellent agreement between EL and PL, and the assignment of the excitonic (E_{11}) and trionic ($E_{11'T}$) emissions are consistent. Regarding the functionalized nano-tubes, the neutral defect emission (E^*) observed in EL does fit to the E_{11}^{*-} band in the PL spectrum, however, this band also appears in the chemical-doping study of the pristine nanotubes. Moreover, the charged defect emission, seen in EL under electrostatic gating (E^*_T), has no equivalent peak in the PL of doped functionalized nanotubes. Fortunately, the electro-luminescence spectra from gate-controlled single-tube devices under vacuum and at low-temperature in correlation with the charge transport characteristics is conclusive in itself.

METHODS SECTION

Dispersion and Functionalization of SWCNTs. The (7, 5) single-walled carbon nanotubes dispersion was prepared in the procedure as reported in our previous work.[23] For detailed description, 100 mg of the raw material soot (CoMoCAt, Sigma-Aldrich) and 100 mg of the polymer poly(9,9-di-n-octylfluorenyl-2,7-diyl) (PFO, Sigma-Aldrich) were dissolved in 100 mL of toluene. The suspension then went through a sonication treatment for 2 h using a titanium sonotrode (Bandelin, ~20% power) while the suspension was placed in a water-circulation bath to aid cooling. After sonication, the suspension was centrifuged for 2 h at 20 000g. To generate the starting suspensions for size-exclusion separation, the supernatant was concentrated to ~10 mL by evaporating ~90 mL of toluene. Semipreparative size exclusion chromatography was performed using Toyopearl HW-75 resin (Tosoh Bioscience) filled into a glass column having 16 mm inner diameter and 20 cm length. For length sorting, 10 mL of starting suspension was loaded onto the column, and flowed through the gel under gravity, at a flow rate of ~2 mL/min, with toluene used as the eluent. Fractions with different length distributions were collected in 3−4 mL portions. (6, 5) dispersion was produced in the similar way except polymer poly[(9,9-dioctylfluorenyl-2,7-diyl)-alt-co-(6,6′-{2,2′-bipyridine})] (PFO-BPy) was used.[60] For the functionalization, 100 μg of 3,5-dichlorophe-nyldiazonium tetrafluoroborate was added to 1 mL of a fraction with a suitable tube length (~500 nm for this work) and heated on a heated plate, just below the boiling point of toluene, for 1 h. Right after the functionalization process, PL spectra were measured by using a home-built setup as described elsewhere.[61] UV−vis−NIR absorption spectra were recorded on a Varian Cary 500 spectrophotometer. Photo-luminescence excitation maps were measured in the emission range of ~900−1700 nm and excitation range of 500−950 nm (scanned in 3 nm steps) using a modified Fourier-transform-infrared (FTIR) spectrometer (Bruker IFS66) equipped with a liquid nitrogen-cooled Ge-photodiode and a monochromatized excitation light source with a 250 W halogen lamp. The PL intensity was corrected for wavelength-dependent excitation intensity and the instrumental response of the spectrometer.

Device Fabrication and SWCNTs Deposition. The devices with graphene electrodes were fabricated from monolayer graphene on 300 nm thermal SiO_2 on p-type (B-doped) Si (Graphenea). Three electron-beam lithography steps (Leo 1530, Raith ElphyPlus) with proximity correction were required for patterning electrodes. Poly(methyl methacrylate) (PMMA 950 K in Anisol) was used as a positive resist. Samples were spin-casted with resist and prebaked on a hot plate for 3 min at 150 °C. After the e-beam patterning, cold development was followed in a solution of methyl isobutyl ketone (MIBK) and isopropanol (1:3) for 30 s. Samples were rinsed with isopropanol, dried in a stream of nitrogen, and annealed at 90 °C for 1 min on a hot plate. In the first step of e-beam lithography, markers were defined, deposited with 50 nm tungsten by sputtering technique (Bestec), and lifted off in acetone. In the second step, graphene strips were defined, and the remaining graphene apart from the PMMA covered strips was etched via oxygen plasma (RIE Oxford Plasmalab 80 plus). The graphene strips have channel lengths of 100 nm and were perforated with holes to minimize the contact resistance. Metal leads were defined in the last e-beam lithography step and subsequently deposited with 3 nm chromium and 42 nm palladium by sputtering. The lift-off process was performed in acetone to complete the fabrication. For the (6, 5) devices with metallic source-drain electrodes, only one e-beam lithography step is required to define the Pd source-drain electrodes with a 200 nm gap size. The lift-off process is done in acetone with mild sonication. The p-doped silicon substrate was used as global back-gate electrodes in all devices. Single chirality SWCNTs were integrated into the device using electric field-assisted dielectrophoresis.[26] The toluene-based suspen-sion which has been used for absorption spectra and photo-luminescence excitation map measurement in Figure 1 was further diluted by a factor of 10−20 to obtain individual SWCNTs. Fifteen μL suspension was drop cast onto the device array and DC bias between 0.1 and 2 V was applied on the common drain and the back-gate electrodes by using Agilent 33250 function generator for 3 min. The samples were rinsed with toluene several times to remove excess polymer residue and dried with a nitrogen stream. The devices were annealed at 70 °C for 15 min to improve contact resistance before performing preliminary transport measurements. To confirm the successful deposition of SWCNT(s) between source-drain electrode pairs, transfer characteristics of the device were conducted at ambient conditions with a probe station using Agilent 4155C semiconductor parameter analyzer. For biasing, we used separate source-measure-ment units (SMU) for each terminal: source, drain, and gate. The bias applied to the source and gate electrode was referenced to the drain potential.

Optical Cryostat and Electroluminescence Spectroscopy Setup. Samples were mounted on a home-built holder and loaded into a 4−500 K continuous-flow, sample-in-vacuum, optical cryostat (MicrostatHiResII, Oxford Instruments). On-chip devices were electrically wire-bonded to the palladium pads on the sample holder. The samples were vacuum annealed (below 10^{-6} mbar) in $situ$ at 70−120 °C via the integrated heater (ITC 503) and electroluminescence measurements were followed without breaking the vacuum. SWCNT devices were driven by using Agilent 4155B semiconductor parameter analyzer where source-drain electrodes were operated in constant-current mode, whereas the gate electrode was running in constant-voltage mode. The cryogenic temperature was reached by introducing liquid nitrogen or liquid helium. The optical cryostat was positioned under a customized optical microscope (Zeiss Axiotech Vario) where the light from the emitter was collected with a Zeiss objective LD Plan-Neofluar (40×/NA0.6). The light was focused by a silver-coated off-axis parabolic mirror (MPD149-P01, f/4, Thorlabs) into an imaging spectrograph (Acton SP-2360, f/3.9, Princeton Instruments) and dispersed via a diffraction grating (85 g/mm, 1.35 μm) onto a liquid-nitrogen-cooled 1024 × 1 pixels linear InGaAs photodiode array (PyLon-IR, Princeton Instruments), sensitive from 950 to 1610 nm. Wavelength calibration of the 1D InGaAs detector was performed by using the built-in function with a mercury−argon calibration light source (WITec). To compensate for the wavelength-dependent intensity scaling factor of the setup, the spectral sensitivity curve was

acquired. The calibration of the spectral sensitivity and some more detail of the setup was described elsewhere in our previous report. The precise and stable positioning of the emitter was achieved via a motorized XY scanning stage (8MTF, Standa) along with a high-precision objective piezo scanner (P-721 PIFOC, PI) for tuning the focusing distance.

Redox-Chemical Doping of SWCNT Suspensions. Redox-chemical doping (p-doped) of the SWCNT suspensions was performed by titration with gold(III) chloride solution (Sigma-Aldrich, ≥ 99.99%) using 10:1 (v/v) toluene to acetonitrile solvent mixture for both SWCNT suspensions and redox solutions. The addition of acetonitrile is required to improve gold(III) chloride solubility. The PL spectra were recorded using a custom-built setup, with a supercontinuum light source (SuperK Extreme EXR-15, NKT Photonics), equipped with a variable band-pass filter (SuperK Varia, NKT Photonics). 650 nm (640 nm −660 nm) laser light was used for the excitation of the SWCNTs in the visible region. A cuvette with a 10 mm path length, containing the SWCNT suspension ($OD(S_1)$ = 0.2, 500 μL starting volume) was placed in the focus of the excitation laser. Near-infrared PL was collected at 90° off-axis. Scattered excitation light was blocked from entering the spectrograph by a 900 nm long-pass filter. After spectrally dispersing the emitted fluorescence using an F/4, 303 mm focal length Shamrock (SR-303i, Andor) grating spectrograph with a 150 lines/mm grating, the PL was detected by a thermo-electrically cooled InGaAs array (iDus PDA DU49−1.7, Andor). Spectra were corrected for dilution induced by the addition of gold chloride solution, as well as for grating and detector sensitivities.

Calculations of Normal-Mode Frequencies. Density functional theory (DFT) calculations using the PBE functional and the def2-SVP basis set[62] were performed applying the program package TURBOMOLE,[63] with the following settings: grid 4, scfconv 7. The resolution of the identity approximation was used to accelerate the calculations of the Coulomb interactions. As a model system for 3,5-dichlorobenzene-functionalization, a $C_{54}H_{18}$ flake was used as a substrate. For the adsorption, three different situations were considered. (a) adsorption of a 3,5-dichlorophenyl anion, (b) the same in the presence of hydrogen close by, and (c) adsorption of a 3,5-dichlorophenyl radical. The structure of the flake was optimized under the assumption of C_{6h} symmetry, the structures with adsorbates in C_1 symmetry. For all optimized structures, analytical vibrational frequencies were calculated. In none of the cases, negative force constants were observed proving that all structures are local minima.

ASSOCIATED CONTENT

● Supporting Information

The Supporting Information is available free of charge at https://pubs.acs.org/doi/10.1021/acsnano.2c03083.

> Additional data in Figures S1−S10 on photoluminescence excitation maps, length distribution, electrical characterization, electroluminescence spectra and analysis, and normal-mode frequency analysis (PDF)

AUTHOR INFORMATION

Corresponding Author

Ralph Krupke − *Institute of Quantum Materials and Technologies, Karlsruhe Institute of Technology, 76021 Karlsruhe, Germany; Institute of Materials Science, Technische Universität Darmstadt, 64287 Darmstadt, Germany; Institute of Nanotechnology, Karlsruhe Institute of Technology, 76021 Karlsruhe, Germany;* ● orcid.org/0000-0001-8427-8592; Email: ralph.krupke@kit.edu

Authors

Min-Ken Li − *Institute of Quantum Materials and Technologies, Karlsruhe Institute of Technology, 76021 Karlsruhe, Germany; Institute of Materials Science,*

Technische Universität Darmstadt, 64287 Darmstadt, Germany

Adnan Riaz − *Institute of Materials Science, Technische Universität Darmstadt, 64287 Darmstadt, Germany; Institute of Nanotechnology, Karlsruhe Institute of Technology, 76021 Karlsruhe, Germany*

Martina Wederhake − *Institute of Physical and Theoretical Chemistry, Julius Maximilian University Würzburg, Würzburg 97074, Germany*

Karin Fink − *Institute of Nanotechnology, Karlsruhe Institute of Technology, 76021 Karlsruhe, Germany*

Avishek Saha − *Center for Integrated Nanotechnologies, Materials Physics and Applications Division, Los Alamos National Laboratory, Los Alamos, New Mexico 87545, United States*

Simone Dehm − *Institute of Nanotechnology, Karlsruhe Institute of Technology, 76021 Karlsruhe, Germany*

Xiaowei He − *Center for Integrated Nanotechnologies, Materials Physics and Applications Division, Los Alamos National Laboratory, Los Alamos, New Mexico 87545, United States; Present Address:* Key Laboratory for the Physics and Chemistry of Nanodevices and Center for Carbon-Based Electronics, School of Electronics, Peking University, Beijing100871, China

Friedrich Schöppler − *Institute of Physical and Theoretical Chemistry, Julius Maximilian University Würzburg, Würzburg 97074, Germany*

Manfred M. Kappes − *Institute of Quantum Materials and Technologies, Karlsruhe Institute of Technology, 76021 Karlsruhe, Germany; Institute of Nanotechnology, Karlsruhe Institute of Technology, 76021 Karlsruhe, Germany; Institute of Physical Chemistry, Karlsruhe Institute of Technology, 76128 Karlsruhe, Germany;* ● orcid.org/0000-0002-1199-1730

Han Htoon − *Center for Integrated Nanotechnologies, Materials Physics and Applications Division, Los Alamos National Laboratory, Los Alamos, New Mexico 87545, United States;* ● orcid.org/0000-0003-3696-2896

Valentin N. Popov − *Faculty of Physics, University of Sofia, 1164 Sofia, Bulgaria*

Stephen K. Doorn − *Center for Integrated Nanotechnologies, Materials Physics and Applications Division, Los Alamos National Laboratory, Los Alamos, New Mexico 87545, United States;* ● orcid.org/0000-0002-9535-2062

Tobias Hertel − *Institute of Physical and Theoretical Chemistry, Julius Maximilian University Würzburg, Würzburg 97074, Germany;* ● orcid.org/0000-0001-7907-4341

Frank Hennrich − *Institute of Quantum Materials and Technologies, Karlsruhe Institute of Technology, 76021 Karlsruhe, Germany*

Complete contact information is available at: https://pubs.acs.org/10.1021/acsnano.2c03083

Author Contributions

The experiments were conceived and designed by R.K., M.L., and F.H. Dispersions with functionalized (7,5) SWCNTs were prepared by F.H., with input from S.K.D. A.S. and X.H. performed functionalization of (6,5) SWCNTs under supervision of S.K.D. and H.H. Devices were fabricated and subjected to charge-transport and electroluminescence measurements by M.L., A.R., and S.D. Photoluminescence measure-

REFERENCES

(1) Knill, E.; Laflamme, R.; Milburn, G. J. A Scheme for Efficient Quantum Computation with Linear Optics. *Nature* **2001**, *409* (6816), 46−52.

(2) Beveratos, A.; Brouri, R.; Gacoin, T.; Villing, A.; Poizat, J.-P.; Grangier, P. Single Photon Quantum Cryptography. *Phys. Rev. Lett.* **2002**, *89* (18), 187901.

(3) Aharonovich, I.; Englund, D.; Toth, M. Solid-State Single-Photon Emitters. *Nat. Photonics* **2016**, *10* (10), 631−641.

(4) Eisaman, M. D.; Fan, J.; Migdall, A.; Polyakov, S. V. Invited Review Article: Single-Photon Sources and Detectors. *Rev. Sci. Instrum.* **2011**, *82* (7), 071101.

(5) Kurtsiefer, C.; Mayer, S.; Zarda, P.; Weinfurter, H. Stable Solid-State Source of Single Photons. *Phys. Rev. Lett.* **2000**, *85* (2), 290−293.

(6) Michler, P.; Kiraz, A.; Becher, C.; Schoenfeld, W. V.; Petroff, P. M.; Zhang, L.; Hu, E.; Imamoglu, A. A Quantum Dot Single-Photon Turnstile Device. *Science* **2000**, *290* (5500), 2282−2285.

(7) Lounis, B.; Moerner, W. E. Single Photons on Demand from a Single Molecule at Room Temperature. *Nature* **2000**, *407* (6803), 491−493.

(8) Avouris, P.; Freitag, M.; Perebeinos, V. Carbon-Nanotube Photonics and Optoelectronics. *Nat. Photonics* **2008**, *2* (6), 341−350.

(9) Högele, A.; Galland, C.; Winger, M.; Imamoğlu, A. Photon Antibunching in the Photoluminescence Spectra of a Single Carbon Nanotube. *Phys. Rev. Lett.* **2008**, *100* (21), 217401.

(10) Khasminskaya, S.; Pyatkov, F.; Słowik, K.; Ferrari, S.; Kahl, O.; Kovalyuk, V.; Rath, P.; Vetter, A.; Hennrich, F.; Kappes, M. M.; Gol'tsman, G.; Korneev, A.; Rockstuhl, C.; Krupke, R.; Pernice, W. H. P. Fully Integrated Quantum Photonic Circuit with an Electrically Driven Light Source. *Nat. Photonics* **2016**, *10* (11), 727−732.

(11) Zhao, H.; Mazumdar, S. Electron-Electron Interaction Effects on the Optical Excitations of Semiconducting Single-Walled Carbon Nanotubes. *Phys. Rev. Lett.* **2004**, *93* (15), 157402.

(12) Hertel, T.; Himmelein, S.; Ackermann, T.; Stich, D.; Crochet, J. Diffusion Limited Photoluminescence Quantum Yields in 1-D Semiconductors: Single-Wall Carbon Nanotubes. *ACS Nano* **2010**, *4* (12), 7161−7168.

(13) Ghosh, S.; Bachilo, S. M.; Simonette, R. A.; Beckingham, K. M.; Weisman, R. B. Oxygen Doping Modifies Near-Infrared Band Gaps in Fluorescent Single-Walled Carbon Nanotubes. *Science* **2010**, *330* (6011), 1656−1659.

(14) Maeda, Y.; Minami, S.; Takehana, Y.; Dang, J.-S.; Aota, S.; Matsuda, K.; Miyauchi, Y.; Yamada, M.; Suzuki, M.; Zhao, R.-S.; Zhao, X.; Nagase, S. Tuning of the Photoluminescence and Up-Conversion Photoluminescence Properties of Single-Walled Carbon Nanotubes by Chemical Functionalization. *Nanoscale* **2016**, *8* (38), 16916−16921.

(15) Kwon, H.; Furmanchuk, A.; Kim, M.; Meany, B.; Guo, Y.; Schatz, G. C.; Wang, Y. Molecularly Tunable Fluorescent Quantum Defects. *J. Am. Chem. Soc.* **2016**, *138* (21), 6878−6885.

(16) Piao, Y.; Meany, B.; Powell, L. R.; Valley, N.; Kwon, H.; Schatz, G. C.; Wang, Y. Brightening of Carbon Nanotube Photoluminescence through the Incorporation of Sp 3 Defects. *Nat. Chem.* **2013**, *5* (10), 840−845.

(17) Janas, D. Perfectly Imperfect: A Review of Chemical Tools for Exciton Engineering in Single-Walled Carbon Nanotubes. *Mater. Horizons* **2020**, *7* (11), 2860−2881.

(18) Miyauchi, Y.; Iwamura, M.; Mouri, S.; Kawazoe, T.; Ohtsu, M.; Matsuda, K. Brightening of Excitons in Carbon Nanotubes on Dimensionality Modification. *Nat. Photonics* **2013**, *7* (9), 715−719.

(19) Ma, X.; Hartmann, N. F.; Baldwin, J. K. S.; Doorn, S. K.; Htoon, H. Room-Temperature Single-Photon Generation from Solitary Dopants of Carbon Nanotubes. *Nat. Nanotechnol.* **2015**, *10* (8), 671−675.

(20) He, X.; Hartmann, N. F.; Ma, X.; Kim, Y.; Ihly, R.; Blackburn, J. L.; Gao, W.; Kono, J.; Yomogida, Y.; Hirano, A.; Tanaka, T.; Kataura, H.; Htoon, H.; Doorn, S. K. Tunable Room-Temperature Single-Photon Emission at Telecom Wavelengths from Sp3 Defects in Carbon Nanotubes. *Nat. Photonics* **2017**, *11* (9), 577−582.

(21) Xu, B.; Wu, X.; Kim, M.; Wang, P.; Wang, Y. Electroluminescence from 4-Nitroaryl Organic Color Centers in Semiconducting Single-Wall Carbon Nanotubes. *J. Appl. Phys.* **2021**, *129* (4), 044305.

(22) Zorn, N. F.; Berger, F. J.; Zaumseil, J. Charge Transport in and Electroluminescence from Sp 3 -Functionalized Carbon Nanotube Networks. *ACS Nano* **2021**, *15* (6), 10451−10463.

(23) Hennrich, F.; Li, W.; Fischer, R.; Lebedkin, S.; Krupke, R.; Kappes, M. M. Length-Sorted, Large-Diameter, Polyfluorene-Wrapped Semiconducting Single-Walled Carbon Nanotubes for High-Density, Short-Channel Transistors. *ACS Nano* **2016**, *10* (2), 1888−1895.

(24) He, X.; Gifford, B. J.; Hartmann, N. F.; Ihly, R.; Ma, X.; Kilina, S. V.; Luo, Y.; Shayan, K.; Strauf, S.; Blackburn, J. L.; Tretiak, S.; Doorn, S. K.; Htoon, H. Low-Temperature Single Carbon Nanotube Spectroscopy of Sp 3 Quantum Defects. *ACS Nano* **2017**, *11* (11), 10785−10796.

(25) Saha, A.; Gifford, B. J.; He, X.; Ao, G.; Zheng, M.; Kataura, H.; Htoon, H.; Kilina, S.; Tretiak, S.; Doorn, S. K. Narrow-Band Single-Photon Emission through Selective Aryl Functionalization of Zigzag Carbon Nanotubes. *Nat. Chem.* **2018**, *10* (11), 1089−1095.

(26) Li, W.; Hennrich, F.; Flavel, B. S.; Dehm, S.; Kappes, M.; Krupke, R. Principles of Carbon Nanotube Dielectrophoresis. *Nano Res.* **2021**, *12* (1). DOI: 10.1007/s12274-020-3183-0.

(27) Gaulke, M.; Janissek, A.; Peyyety, N. A.; Alamgir, I.; Riaz, A.; Dehm, S.; Li, H.; Lemmer, U.; Flavel, B. S.; Kappes, M. M.; Hennrich, F.; Wei, L.; Chen, Y.; Pyatkov, F.; Krupke, R. Low-Temperature Electroluminescence Excitation Mapping of Excitons and Trions in Short-Channel Monochiral Carbon Nanotube Devices. *ACS Nano* **2020**, *14* (3), 2709−2717.

(28) Zheng, Y.; Bachilo, S. M.; Weisman, R. B. Photoexcited Aromatic Reactants Give Multicolor Carbon Nanotube Fluorescence from Quantum Defects. *ACS Nano* **2020**, *14* (1), 715−723.

(29) Settele, S.; Berger, F. J.; Lindenthal, S.; Zhao, S.; El Yumin, A. A.; Zorn, N. F.; Asyuda, A.; Zharnikov, M.; Högele, A.; Zaumseil, J. Synthetic Control over the Binding Configuration of Luminescent Sp3-Defects in Single-Walled Carbon Nanotubes. *Nat. Commun.* **2021**, *12* (1), 2119.

(30) Kwon, H.; Kim, M.; Nutz, M.; Hartmann, N. F.; Perrin, V.; Meany, B.; Hofmann, M. S.; Clark, C. W.; Htoon, H.; Doorn, S. K.; Högele, A.; Wang, Y. Probing Trions at Chemically Tailored Trapping Defects. *ACS Cent. Sci.* **2019**, *5* (11), 1786−1794.

(31) Misewich, J. A. Electrically Induced Optical Emission from a Carbon Nanotube FET. *Science* **2003**, *300* (5620), 783−786.

(32) Freitag, M.; Chen, J.; Tersoff, J.; Tsang, J.; Fu, Q.; Liu, J.; Avouris, P. Mobile Ambipolar Domain in Carbon-Nanotube Infrared Emitters. *Phys. Rev. Lett.* **2004**, *93* (7), 076803.

(33) Chen, J. Bright Infrared Emission from Electrically Induced Excitons in Carbon Nanotubes. *Science* **2005**, *310* (5751), 1171−1174.

(34) Hofmann, M. S.; Noé, J.; Kneer, A.; Crochet, J. J.; Högele, A. Ubiquity of Exciton Localization in Cryogenic Carbon Nanotubes. *Nano Lett.* **2016**, *16* (5), 2958−2962.

(35) Moritsubo, S.; Murai, T.; Shimada, T.; Murakami, Y.; Chiashi, S.; Maruyama, S.; Kato, Y. K. Exciton Diffusion in Air-Suspended Single-Walled Carbon Nanotubes. *Phys. Rev. Lett.* **2010**, *104* (24), 247402.

(36) Vijayaraghavan, A.; Hennrich, F.; Stürzl, N.; Engel, M.; Ganzhorn, M.; Oron-Carl, M.; Marquardt, C. W.; Dehm, S.; Lebedkin, S.; Kappes, M. M.; Krupke, R. Toward Single-Chirality Carbon Nanotube Device Arrays. *ACS Nano* **2010**, *4* (5), 2748−2754.

(37) Yi, X.; Ozawa, H.; Nakagawa, G.; Fujigaya, T.; Nakashima, N.; Asano, T. Single-Walled Carbon Nanotube Thin Film Transistor Fabricated Using Solution Prepared with 9,9-Dioctyfluorenyl-2,7-Diyl-Bipyridine Copolymer. *Jpn. J. Appl. Phys.* **2011**, *50* (7), 070207.

(38) Simpson, J. R.; Roslyak, O.; Duque, J. G.; Hároz, E. H.; Crochet, J. J.; Telg, H.; Piryatinski, A.; Walker, A. R. H.; Doorn, S. K. Resonance Raman Signature of Intertube Excitons in Compositionally-Defined Carbon Nanotube Bundles. *Nat. Commun.* **2018**, *9* (1), 637.

(39) Grimm, S.; Schießl, S. P.; Zakharko, Y.; Rother, M.; Brohmann, M.; Zaumseil, J. Doping-Dependent G-Mode Shifts of Small Diameter Semiconducting Single-Walled Carbon Nanotubes. *Carbon N. Y.* **2017**, *118*, 261−267.

(40) Ozawa, H.; Ide, N.; Fujigaya, T.; Niidome, Y.; Nakashima, N. One-Pot Separation of Highly Enriched (6,5)-Single-Walled Carbon Nanotubes Using a Fluorene-Based Copolymer. *Chem. Lett.* **2011**, *40* (3), 239−241.

(41) Lefebvre, J.; Finnie, P.; Homma, Y. Temperature-Dependent Photoluminescence from Single-Walled Carbon Nanotubes. *Phys. Rev. B* **2004**, *70* (4), 045419.

(42) Galland, C.; Högele, A.; Türeci, H. E.; Imamoğlu, A. Non-Markovian Decoherence of Localized Nanotube Excitons by Acoustic Phonons. *Phys. Rev. Lett.* **2008**, *101* (6), 067402.

(43) Vialla, F.; Chassagneux, Y.; Ferreira, R.; Roquelet, C.; Diederichs, C.; Cassabois, G.; Roussignol, P.; Lauret, J. S.; Voisin, C. Unifying the Low-Temperature Photoluminescence Spectra of Carbon Nanotubes: The Role of Acoustic Phonon Confinement. *Phys. Rev. Lett.* **2014**, *113* (5), 057402.

(44) Nutz, M. *Signatures of Correlations and Interactions in the Optical Spectra of Localized Excitons in Carbon Nanotubes*. Ph.D. thesis, LMU München: München, Germany, 2020.

(45) Tachikawa, H.; Kawabata, H. Electronic States of Aryl Radical Functionalized Graphenes: Density Functional Theory Study. *Jpn. J. Appl. Phys.* **2016**, *55* (6S1), 06GK05.

(46) Gross, E.; Permogorov, S.; Morozenko, Y.; Kharlamov, B. Hot-Exciton Luminescence in CdSe Crystals. *Phys. Status Solidi* **1973**, *59* (2), 551−560.

(47) Pelekanos, N.; Ding, J.; Fu, Q.; Nurmikko, A. V.; Durbin, S. M.; Kobayashi, M.; Gunshor, R. L. Hot-Exciton Luminescence in ZnTe/MnTe Quantum Wells. *Phys. Rev. B* **1991**, *43* (11), 9354−9357.

(48) Zhang, Q.; Liu, X.; Utama, M. I. B.; Zhang, J.; de la Mata, M.; Arbiol, J.; Lu, Y.; Sum, T. C.; Xiong, Q. Highly Enhanced Exciton Recombination Rate by Strong Electron-Phonon Coupling in Single ZnTe Nanobelt. *Nano Lett.* **2012**, *12* (12), 6420−6427.

(49) Cho, C.-H.; Aspetti, C. O.; Turk, M. E.; Kikkawa, J. M.; Nam, S.-W.; Agarwal, R. Tailoring Hot-Exciton Emission and Lifetimes in

(50) Permogorov, S. Hot Excitons in Semiconductors. *Phys. Status Solidi* **1975**, *68* (1), 9−42.

(51) Vamivakas, A. N.; Yin, Y.; Walsh, A. G.; Unlu, M. S.; Goldberg, B. B.; Swan, A. K. Chirality Dependence of the Radial Breathing Phonon Mode Density in Single Wall Carbon Nanotubes. 2006, *arXiv:cond-mat/0609197*. https://arxiv.org/abs/cond-mat/0609197 (accessed 2022/06/06).

(52) Popov, V. N. Two-Phonon Raman Bands of Single-Walled Carbon Nanotubes: A Case Study. *Phys. Rev. B* **2018**, *98* (8), 085413.

(53) Kelley, A. M. Exciton-Optical Phonon Coupling in II-VI Semiconductor Nanocrystals. *J. Chem. Phys.* **2019**, *151* (14), 140901.

(54) Leite, R. C. C.; Scott, J. F.; Damen, T. C. Multiple-Phonon Resonant Raman Scattering in CdS. *Phys. Rev. Lett.* **1969**, *22* (15), 780−782.

(55) Eckstein, K. H.; Hartleb, H.; Achsnich, M. M.; Schöppler, F.; Hertel, T. Localized Charges Control Exciton Energetics and Energy Dissipation in Doped Carbon Nanotubes. *ACS Nano* **2017**, *11* (10), 10401−10408.

(56) Eckstein, K. H.; Oberndorfer, F.; Achsnich, M. M.; Schöppler, F.; Hertel, T. Quantifying Doping Levels in Carbon Nanotubes by Optical Spectroscopy. *J. Phys. Chem. C* **2019**, *123* (49), 30001−30006.

(57) Trerayapiwat, K. J.; Lohmann, S.; Ma, X.; Sharifzadeh, S. Tuning Spin-Orbit Coupling in (6,5) Single-Walled Carbon Nanotube Doped with Sp 3 Defects. *J. Appl. Phys.* **2021**, *129* (1), 014309.

(58) Lohmann, S.-H.; Trerayapiwat, K. J.; Niklas, J.; Poluektov, O. G.; Sharifzadeh, S.; Ma, X. Sp 3 -Functionalization of Single-Walled Carbon Nanotubes Creates Localized Spins. *ACS Nano* **2020**, *14* (12), 17675−17682.

(59) Qu, H.; Wu, X.; Fortner, J.; Kim, M.; Wang, P.; Wang, Y. Reconfiguring Organic Color Centers on the Sp 2 Carbon Lattice of Single-Walled Carbon Nanotubes. *ACS Nano* **2022**, *16* (2), 2077−2087.

(60) Hartmann, N. F.; Pramanik, R.; Dowgiallo, A.-M.; Ihly, R.; Blackburn, J. L.; Doorn, S. K. Photoluminescence Imaging of Polyfluorene Surface Structures on Semiconducting Carbon Nanotubes: Implications for Thin Film Exciton Transport. *ACS Nano* **2016**, *10* (12), 11449−11458.

(61) Lebedkin, S.; Hennrich, F.; Kiowski, O.; Kappes, M. M. Photophysics of Carbon Nanotubes in Organic Polymer-Toluene Dispersions: Emission and Excitation Satellites and Relaxation Pathways. *Phys. Rev. B* **2008**, *77* (16), 1−8.

(62) Schäfer, A.; Horn, H.; Ahlrichs, R. Fully Optimized Contracted Gaussian Basis Sets for Atoms Li to Kr. *J. Chem. Phys.* **1992**, *97* (4), 2571−2577.

(63) *TURBOMOLE*, V7.2; TURBOMOLE GmbH, 2017, http://www.turbomole.com.